



Boychev, K.M., Barakos, G.N., Stejrl, R. and Shaw, S. (2020) High Fidelity Simulations of Supersonic Intakes. In: 2020 AIAA SciTech Forum, Orlando, FL, USA, 06-10 Jan 2020, ISBN 9781624105951 (doi:[10.2514/6.2020-2092](https://doi.org/10.2514/6.2020-2092)).

This is the author's final accepted version.

There may be differences between this version and the published version. You are advised to consult the publisher's version if you wish to cite from it.

<http://eprints.gla.ac.uk/203865/>

Deposited on: 21 November 2019

Enlighten – Research publications by members of the University of Glasgow  
<http://eprints.gla.ac.uk>

# High-Fidelity Simulations of Supersonic Intakes

K. M. Boychev\*, G. N. Barakos†, R. Steijl‡

CFD Laboratory, School of Engineering, University of Glasgow, G128QQ Glasgow, UK

S. Shaw §

MBDA UK Ltd, Filton, Bristol, BS347QW, UK

A parametric study of Multiple Shock Wave Boundary Layer Interaction is presented in this paper. All results were obtained using the in-house CFD solver of Glasgow University. Such interactions often occur in high-speed intakes which have recently seen a renewed interest. Simulations of a multiple shock wave boundary layer interaction in a rectangular duct were first performed and the results were compared to the experiments. Using the same numerical setup a parametric study investigating the effect of Mach number, Reynolds number and confinement on the baseline solution was then performed. Efficiency metrics were also defined to quantify the interactions. The results show that Reynolds-stress based turbulence models are better suited than linear models. The corner separations affect the separation at the centreline which in turn alters the structure of the initial shock and the subsequent interaction. Reduced confinement is found to be beneficial for higher pressure recovery. Finally, results for a more realistic geometry (fore-body with an intake) featuring an oblique and multiple shock wave boundary layer interactions are presented.

## Nomenclature

### Latin

- $u$  = streamwise velocity component (m/s)  
 $h$  = duct height or half-height (context specific) (m)  
 $L$  = fore-body length (m)  
 $p$  = static pressure (Pa)  
 $p_0$  = stagnation pressure (Pa)  
 $M$  = Mach number  
 $I$  = turbulence intensity  
 $Re_h$  = Reynolds number based on the duct half-height

### Greek

- $\delta$  = boundary layer thickness (mm)  
 $\mu_t/\mu$  = ratio of eddy viscosity to molecular viscosity  
 $\delta/h$  = ratio of boundary layer thickness to duct half height (flow confinement)

### Subscripts and superscripts

- $(.)_u$  = inlet quantity  
 $(.)_r$  = quantity at the start of the interaction (initial pressure rise)  
 $(.)_\infty$  = free-stream quantity

### Acronyms

---

\*PhD Student, CFD Laboratory, School of Engineering, Email: k.boychev.1@research.gla.ac.uk

†Professor, MAIAA, MRAS, CFD Laboratory, School of Engineering, Email: George.Barakos@glasgow.ac.uk

‡Senior Lecturer, CFD Laboratory, School of Engineering, Email: Rene.Steijl@glasgow.ac.uk

§Senior Principal Aerodynamicist, MBDA UK Ltd, Email: scott.shaw@mbda-systems.com

EARSM	=	Explicit Algebraic Reynolds Stress Model
FD	=	Flow Distortion
(M)SWBLI	=	(Multiple) Shock Wave Boundary Layer Interaction
RANS	=	Reynolds Averaged Navier Stokes
SST	=	Shear Stress Transport
TPR	=	Total Pressure Recovery
CFD	=	Computational Fluid Dynamics
LES	=	Large Eddy Simulation
SAS	=	Scale Adaptive Simulation
DES	=	Detached Eddy Simulation
DDES	=	Delayed Detached Eddy Simulation
IDDES	=	Improved Delayed Detached Eddy Simulation

## I. Introduction

THE interaction of a shock wave with a boundary layer (SWBLI) occurs in a variety of devices such as supersonic wind tunnel diffusers and supersonic (high-speed) intakes. Of particular interest are SWBLIs in supersonic intakes. SWBLIs inside high-speed intakes alter the flow significantly and can affect engine performance. The intake must maintain satisfactory performance under off-design conditions. Such conditions include but are not limited to operating above and below the design Mach number and operating at varying pitch and roll angles. For a particular combination of flight conditions formation of multiple SWBLIs inside the intake is possible. Multiple SWBLIs are often referred to as shock trains or pseudo-shocks. Although these terms are used, at times, interchangeably, the term shock train refers to the series of shocks and the pseudo-shock term refers to the entire region of pressure rise (Matsuo et al. [1]). The region downstream of the shock train region is termed the mixing region. The end of this region is often determined by the maximum of the wall pressure. In addition to multiple SWBLIs, oblique SWBLIs and reflected shocks are often present within the intake. Figure 1 shows a schematic diagram of a multiple normal SWBLI in a rectangular duct/intake.

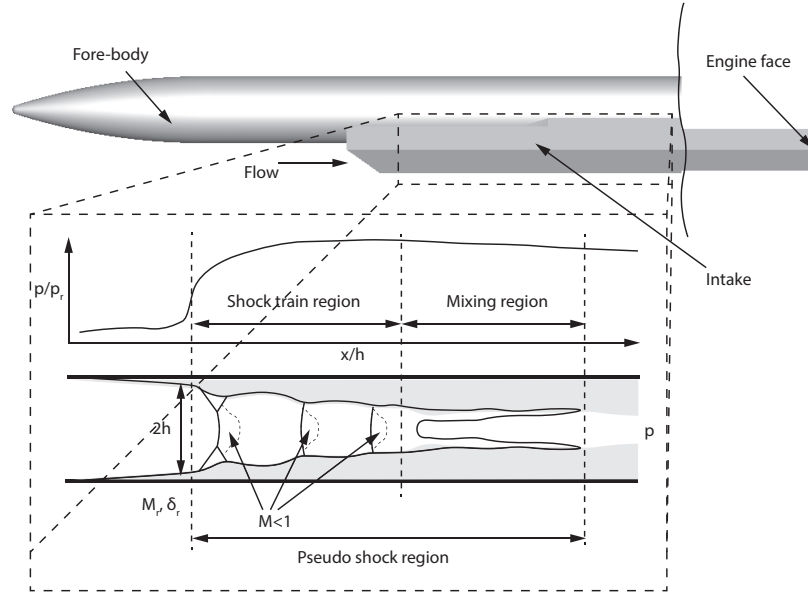


**Fig. 1 Schematic of a multiple shock wave boundary layer interaction in a rectangular duct/intake**

For the multiple normal SWBLI, sketched in Figure 1, the first shock imparts an adverse pressure gradient on the incoming boundary layer developing on the walls of the rectangular duct/intake. If the adverse pressure gradient and wall stresses are large enough, the boundary layer separates and a recirculating flow region forms. This region leads to the formation of oblique compression shocks (leading and trailing legs) which eventually join with the first shock to form a  $\lambda$ -shock structure. Higher Mach numbers downstream of the first shock are present near the corners of the duct, as the  $\lambda$ -shock structures on adjacent walls interact (Handa et al. [2]). The result of their interaction is a weaker adverse

pressure gradient in the corners of the duct compared to the centerline. From the bifurcation (or triple) point formed from the  $\lambda$ -shock structure, a secondary shear layer can develop in the form of a slip line. Downstream of the first shock, the flow is subsonic, however, the local streamline curvature re-accelerates the flow. Due to the curvature, the supersonic flow downstream of the trailing leg of the shock turns towards the wall. Depending on how sudden the turn is (governed by the ratio of boundary layer thickness  $\delta_r$  to the duct half-height  $h$ ) the flow may again become supersonic and promote the formation of multiple SWBLIs (MSWBLIs). For high Mach numbers ( $M_r$ ) the effect of flow confinement ( $\delta_r/h$ ) on the MSWBLI formation is less important than the effect of Mach number. At high Mach numbers, MSWBLIs form even under low flow confinement. As the Mach number or flow confinement increases the SWBLI undergoes a transition from a single normal shock, to multiple normal shocks, to multiple oblique shocks. Multiple oblique shocks are almost exclusively observed at high Mach numbers. The transition from single to multiple SWBLI is accompanied by an increase of the interaction length. A robust numerical method capable of predicting multiple SWBLIs with a reasonable degree of accuracy is therefore required to study MSWBLIs within high-speed intakes. The numerical method must be able to accurately resolve the corner flows present in ducts/intakes. Overestimation of the corner flows can lead to overestimation of pressure oscillations at the wall of the intake. Accurate prediction of the corner flow is also very important at high levels of flow confinement. Current efforts in LES require reduction of the Reynolds number and although they capture the initial pressure rise well, downstream pressure is underpredicted most likely due to incorrect boundary layer growth rate. Hybrid RANS/LES methods such as SAS and DES in different formulations rely on linear eddy-viscosity models in the RANS regions. Since the RANS regions are near the wall, where secondary flows are present, the linear eddy-viscosity models fail to accurately predict the corner flows. The objective of this paper is to investigate the effect of Mach number ( $M_u$ ), Reynolds number ( $Re_h$ ), and level of flow confinement ( $\delta_r/h$ ) on a MSWBLI interaction using non-linear eddy-viscosity model. Section II discusses the numerical method used in this work. Section III first presents a validation of the employed CFD solver by comparing results to a reference MSWBLI case. The section then quantifies the effect of each parameter ( $M_u$ ,  $Re_h$ ,  $\delta_r/h$ ) on the reference case. Five additional MSWBLI cases are considered, each at different combinations of the above parameters, and efficiency metrics are calculated for each interaction. Finally, results for the combined internal-external flow around a fore-body intake geometry are presented in section IV.

## II. Numerical method

The Helicopter Multi-Block (HMB3) [3, 4] code is used in the present work. HMB3 solves the Unsteady Reynolds Averaged Navier-Stokes (URANS) equations in integral form using the Arbitrary Lagrangian Eulerian (ALE) formulation for time-dependent domains, which may include moving boundaries. The Navier-Stokes equations are discretised using a cell-centred finite volume approach on a multi-block grid. The spatial discretisation of these equations leads to a set of ordinary differential equations in time

$$\frac{d}{dt} (\mathbf{W}_{i,j,k} V_{i,j,k}) = -\mathbf{R}_{i,j,k} (\mathbf{W}_{i,j,k}), \quad (1)$$

where  $i,j,k$  represent the cell index,  $\mathbf{W}$  and  $\mathbf{R}$  are the vectors of conservative flow variables and flux residual respectively, and  $V_{i,j,k}$  is the volume of the cell  $i,j,k$ . To evaluate the convective fluxes Osher [5] approximate Riemman solver is used, while the viscous terms are discretised using a second order central differencing spatial discretisation. The Monotonic Upwind Scheme for Conservation Laws, which is referred to in the literature as the MUSCL approach and developed by van Leer [6], is used to provide high-order accuracy in space. The HMB3 solver uses the alternative form of the van Albada limiter [7] being activated in regions where large gradients are encountered mainly due to shock waves, avoiding the non-physical spurious oscillations. An implicit dual-time stepping method is employed to perform the temporal integration, where the solution is marching in pseudo-time iterations to achieve a fast convergence, which is solved using a first-order backward difference. The linearized system of equations is solved using the Generalised Conjugate Gradient method with a Block Incomplete Lower-Upper (BILU) factorisation as a pre-conditioner [8]. To allow an easy sharing of the calculation load for a parallel job, multi-block structured grids are used. Various turbulence models are available in the HMB3 solver, including several one-equation, two-equation, three-equation, and four-equation turbulence models. Furthermore, Large-Eddy Simulation (LES), Detached-Eddy Simulation (DES), Delayed-Detached-Eddy Simulation (DDES), Improved-Delayed-Detached-Eddy Simulation (IDDES), and Scale-Adaptive-Simulation (SAS) are also available. In the present work the fully-turbulent  $k - \omega$  EARSIM [9, 10] turbulence model is used.

### III. Validation and parameteric study of shock trains

#### A. Description of the target experiment for validation

For the shock train simulations performed, the multiple SWBLI experiments by Carroll and Dutton [11–16] is targeted for comparison. In the experiment, a 750 mm long rectangular test section was used with LDV measurements beginning at  $x_r = 264.8$  mm (the approximate location of the first normal shock) and extending downstream, at variable intervals over 400 mm. The top and bottom wall of the rectangular test section had a divergence angle of 0.13 deg. From the boundary layer measurements the height of the rectangular test section at  $x_r = 264.8$  mm is  $2h_r = 33.75$  mm. The width of the section is  $w = 76.2$  mm and is constant throughout. Over the length of the LDV measurements (400 mm) starting from  $x = 264.8$  mm, both the upper and lower walls diverge by 0.91 mm. The Mach number before the interaction was  $M_r = 1.61$  and the unit Reynolds number  $Re = 3.0 \times 10^7 \text{ m}^{-1}$ . The Reynolds number based on the half-height of the duct at the inlet ( $x = 0$ ) is, therefore,  $Re_h = 4.88 \times 10^5$ . A schematic of the experimental setup is shown in Figure 2 below.

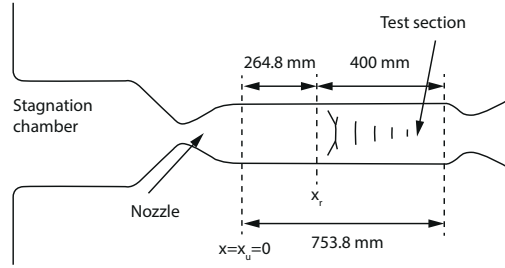


**Fig. 2 Schematic diagram of the experimental setup used by Carroll et al. [11–16]**

Additional simulations of shock trains were compared to the experiment by Sun et al. [17] and the LES of Fievet et al. [18], the results of which are discussed briefly in the results section.

#### B. Numerical setup

A numerical domain extending from  $x = 0$  to  $x = 753.8$  mm was used for the shock train simulations of the experiment by Carroll et al. [11]. The domain was non-dimensionalised by the duct half-height at  $x = 0$ . Figure 3 shows a schematic of the numerical setup.

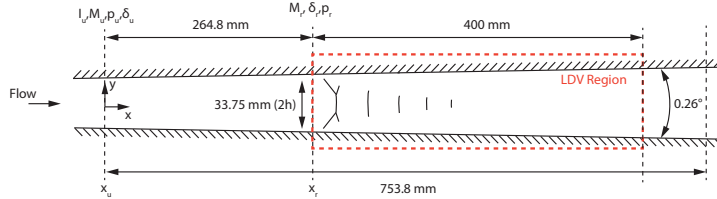


**Fig. 3 Schematic diagram of the numerical setup for the shock train simulations**

##### 1. Computational grids

For the shock train validation simulations, the domain was discretised with 76 cells across its height  $h$ . The non-dimensional distance at the wall was  $y^+ \leq 1$  with at least 10 cells in the viscous sublayer ( $y^+ < 10$ ). To achieve grid convergence, the grid was refined in the streamwise direction. The coarse, medium and fine grids had the same  $y$ - and  $z$ -spacing but 714, 1199, and 2113 cells in the  $x$ -direction. An additional grid with the same  $x$ -spacing as the fine grid but with reduced  $y$ - and  $z$ -spacing was considered. A grid with the same  $y$ - and  $z$ -resolution as the medium grid featuring an extended streamwise refinement region was used for the parametric studies. The extended refinement region allowed for shock train movement due to varying inlet-outlet conditions. The parameters for all grids are shown in table 1.

**Table 1** Grid parameters for the shock train simulations; \* - grid with extended refinement; dash indicates stretching

Grid	min $\Delta x/h$	$\Delta y/h$	Points
Medium	0.02	$1.0 \times 10^{-5}$ -0.05-0.07	$8.93 \times 10^6$
Fine	0.02	$1.0 \times 10^{-5}$ -0.05-0.07	$14.59 \times 10^6$
Veryfine	0.01	$1.0 \times 10^{-5}$ -0.03-0.04	$19.12 \times 10^6$
Medium*	0.02	$1.0 \times 10^{-5}$ -0.05-0.07	$14.61 \times 10^6$

## 2. Boundary conditions

A uniform profile of the flow variables was specified at the inlet of the computational domain where the Mach number, turbulence intensity, and eddy viscosity ratio were set to  $M_u = 1.69$ ,  $I_u = 0.01$  (1 %), and  $\frac{\mu_t}{\mu} = 10$  respectively. This allowed a boundary layer to develop on its own downstream of the inlet. The Mach number at the inlet,  $M_u$  was higher than the experimental one (just upstream of the shock train) to take into account the boundary layer growth upstream of the shock train. This ensured that the Mach number before the shock train  $M_r$  matched the experiments as closely as possible. The higher Mach number at the inlet was accompanied by an adjustment of the pressure  $p$  at the outlet. Increasing or decreasing the pressure at the outlet moves the shock train upstream or downstream to a lower or higher level of confinement ( $\delta_r/h$ ). Both adjustments were necessary to match the Mach number  $M_r$  and the confinement  $\delta_r/h$  simultaneously. A first-order extrapolation of the variables at the outlet was performed except where the flow is subsonic. At those locations, the outlet pressure  $p$  was specified. Adiabatic wall boundary conditions were used at all wall boundaries. Symmetry boundary conditions at the  $x - z$  and  $x - y$  symmetry planes were applied after previous investigations showed no flow asymmetry or sensitivity of the results to this modelling assumption. Only a quarter of the domain was used for the subsequent shock train simulations.

## 3. Validation cases

Table 2 lists the parameters for the shock train simulations of the experiment by Carroll et al. [11]. The flow properties at the inlet and the onset of the interaction are reported in the table. Experimental measurements begin at the location of the start of the interaction  $x_r$ .

**Table 2** Shock train validation cases

Grid	$I_u$ %	$M_u$	$M_r$	$\delta_r$ mm	$\delta_r/h$	$x_r/h$	$p/p_u$	$p/p_r$	Turbulence model
Medium	1.0	1.69	1.6216	5.1444	0.3163	26.3911	2.4776	2.3337	k- $\omega$ EARSM
Fine	1.0	1.69	1.6160	4.9858	0.3065	26.04190	2.4776	2.2329	k- $\omega$ EARSM
Veryfine	1.0	1.69	1.6163	4.6325	0.2848	25.69533	2.4776	2.2320	k- $\omega$ EARSM
Experiment [11]			1.610	5.4000	0.3200	0		2.2309	

## 4. Parametric cases

All parametric simulations were performed on the medium grid with extended refinement using the k- $\omega$  EARSM turbulence model. To investigate the effects of Reynolds number  $Re_h$  and Mach number  $M_u$  on the shock train, first the shock train was simulated at inlet-outlet conditions corresponding to the experiment by Carroll et al. [11]. Two additional simulations were then performed at the same inlet-outlet pressure ratio of  $p/p_u = 2.4776$  and lower Mach number  $M_u$  and Reynolds number  $Re_h$ . The difference in Mach number and Reynolds number between the reference simulation and the simulations at lower  $M_u$  and lower  $Re_h$  are  $\Delta M_u \approx 0.1$  and  $\Delta Re_h \approx 4.4 \times 10^5$ . A simulation at a lower  $\delta_r/h$  was also performed. To decrease the  $\delta_r/h$  from the reference value the outlet pressure was increased by 12%. For the remaining parametric simulations, a Latin hypercube approach was used to generate combinations of inlet Mach number  $M_u$ , outlet pressure percentage  $\eta$ , and Reynolds number  $Re_h$ . The upper and lower limits for each parameter were set to  $1.5 \leq M_u \leq 3.0$ ,  $0.6 \leq \eta \leq 0.9$ , and  $1.0 \times 10^4 \leq Re_h \leq 1.0 \times 10^6$ , where  $\eta$  is defined as a percentage of the pressure rise across a normal shock at a pre-shock Mach number of  $M_u$ . This approach was chosen as the pressure at

the outlet affects the level of flow confinement ( $\delta_u/h$ ), e.g. for an increasing outlet pressure the shock train will move upstream to a lower level of flow confinement and vice-versa. Table 4 lists the parameters for the shock train parametric simulations and Figure 4 shows the parameters in  $M_u-Re_h-p$  space.

**Table 3 Shock train parametric cases**

Case	$Re_h$	$M_u$	$M_r$	$\delta_r$ mm	$\delta_r/h$	$x_r/h$	$p/p_u$	$p/p_r$	$\eta$
Ref.	$4.88 \times 10^5$	1.6900	1.6220	5.0569	0.3107	26.3911	2.4776	2.2485	0.7827
Experiment [11]			1.6100	5.4000	0.3200	0		2.2309	
Ref. Low $M_u$	$4.88 \times 10^5$	1.5900	1.5361	3.1178	0.1917	14.9562	2.4776	2.2883	0.8902
Ref. Low $Re_h$	$4.88 \times 10^4$	1.6900	1.5723	4.9898	0.3067	15.3380	2.4776	2.0781	0.7827
Ref. Low $\delta_r/h$	$4.88 \times 10^5$	1.6900	1.6442	3.2233	0.1982	15.5978	2.7818	2.5543	0.8788
A	$3.54 \times 10^5$	1.6202	1.5402	5.8658	0.3606	30.6827	2.1393	1.8783	0.7387
B	$8.74 \times 10^5$	1.7355	1.6861	5.0930	0.3131	29.3673	2.5642	2.3616	0.7661
C	$2.19 \times 10^5$	1.8898	1.8144	4.1301	0.2539	18.2247	3.1774	2.8186	0.7944
D	$6.24 \times 10^5$	2.0360	1.9827	3.8275	0.2353	18.9103	3.3509	3.0631	0.7176
E	$2.41 \times 10^5$	2.1567	2.0970	2.7783	0.1708	10.9736	4.3285	3.8917	0.8229

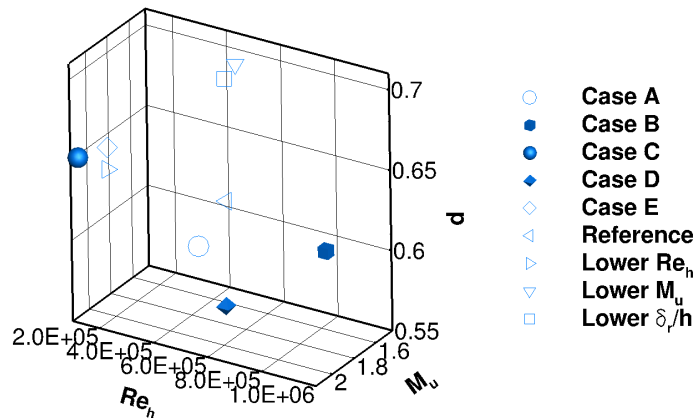


**Fig. 4 Shock train cases in  $M_u-Re_h-p$  parameter space**

All simulations were initialized with a normal shock, at a pre-shock Mach number of  $M_u$ , placed near the end of the domain and were allowed to converge to at least 5 orders of magnitude in the flux residuals.

## C. Results and discussion

### 1. Validation cases

Previous numerical investigations of multiple shock wave boundary layer interactions showed that the fully turbulent  $k-\omega$  EARSMS turbulence model captures the wall pressure well. Figure 5 shows the wall pressure (a) and Mach number contours at the midplane for the medium (b), fine (c) and very fine (d) grids obtained with the  $k-\omega$  EARSMS turbulence model. Note that the solution is mirrored across the  $x-z$  plane. The model slightly underpredicts the wall pressure at the beginning of the interaction which is attributed to the larger predicted separation at the foot of the initial shock. Due to the ability of the model to account for the secondary flows arising in the vicinity of a corner smaller corner separations are predicted by the model and the wall pressure is free from oscillations. The secondary flows tend to suppress the corner separations. The linear  $k-\omega$ ,  $k-\omega$  BSL,  $k-\omega$  SST turbulence models were found to overpredict the size of the corner separations leading to noticeable oscillations of the wall pressure. The difference in the onset of the interaction  $x_r$  between the fine and very fine was  $< 0.7\%$  of the domain length. Consistent prediction of the wall pressure profile

was observed for all grids.

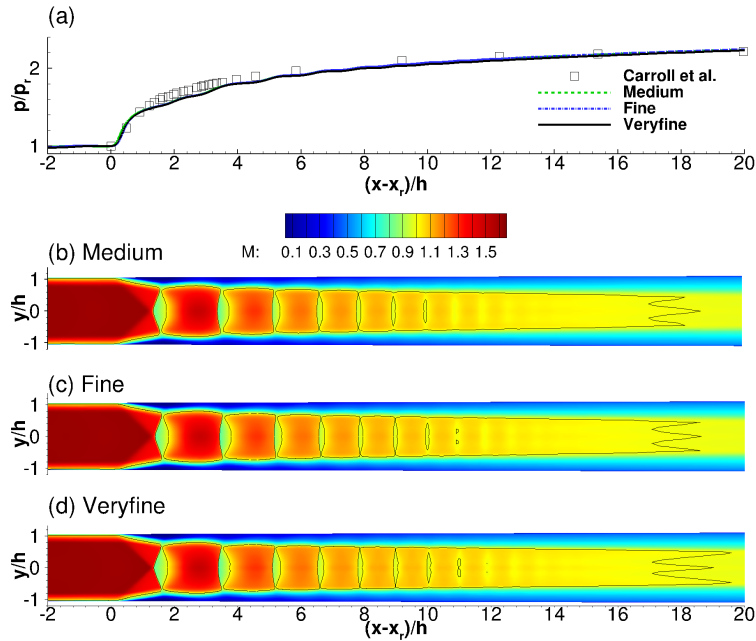


**Fig. 5** Wall pressure (top) and Mach number contours (bottom) for the medium, fine, and veryfine grids with the  $k-\omega$  EARSM turbulence model

Figure 6 shows the wall pressure from the additional  $k-\omega$  EARSM simulations of the experiment of Sun et al. [17] and the experiments reported in Fievet et al. [18].

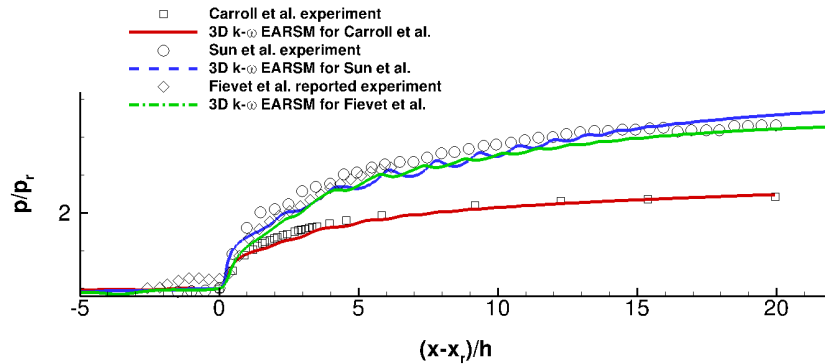


**Fig. 6** Wall pressure (top) and Mach number contours (bottom) for the medium, fine, and veryfine grids with the  $k-\omega$  EARSM turbulence model

Having established confidence in the employed models, CFD codes, and mesh sizes a parametric study investigation of MSWBLIs was also considered.

## 2. Parametric cases

The wall pressure and Mach number contours for the cases at lower Mach and Reynolds numbers are shown in Figure 7. The inlet-outlet pressure ratio for both cases is constant and equal to the pressure ratio of the reference case. The shock train length increased considerably for the case at lower  $Re_h$ . The Mach number contours indicate that the

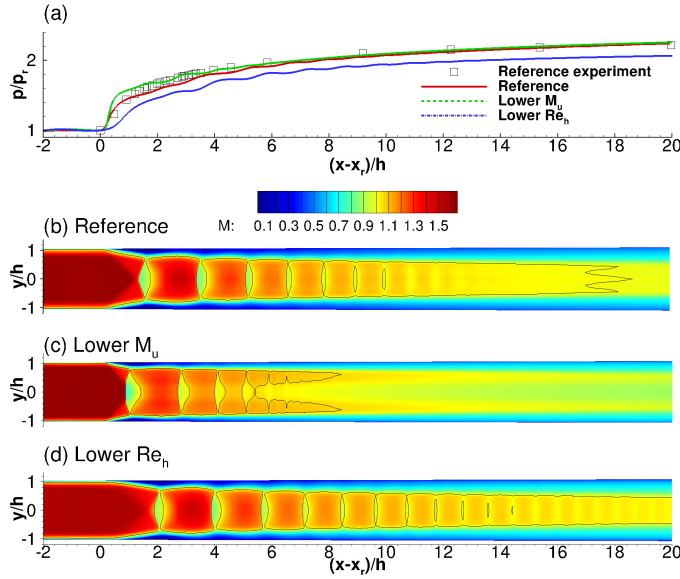


**Fig. 7** Wall pressure (top) and Mach number contours (bottom) for reference and reduced  $M_u$  and  $Re_h$  cases

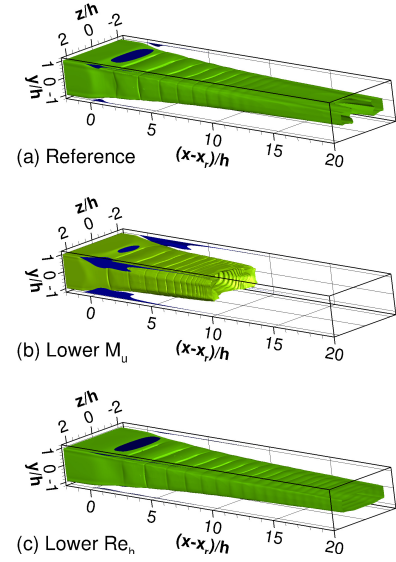


**Fig. 8** Iso-surfaces of  $M = 1.0$  (shaded green) and  $u/V_u = -1 \times 10^{-3}$  (shaded blue) for the reference and reduced  $M_u$  and  $Re_h$  cases

supersonic core flow region extends further downstream. There is no distinct termination of this region as observed in the other two cases. The onset of the pressure rise begins at  $x_r/h = 15.3380$ . The difference with the reference case amounts to  $\approx 24\%$  of the domain length. Although the location of the onset moves upstream for the low  $Re_h$  case, both the reference, and the low  $Re_h$  cases have similar levels of flow confinement -  $\delta_r/h = 0.3107$  and  $\delta_r/h = 0.3067$ . The pre-shock Mach number difference between the two cases is  $\approx 3\%$ . Figures 8 and 9 show the sonic and separation iso-surfaces and the shear stress visualised with friction lines on the wall. Both the reference and the lower  $Re_h$  cases feature large separation on the top and bottom walls with less pronounced corner separations for the latter.

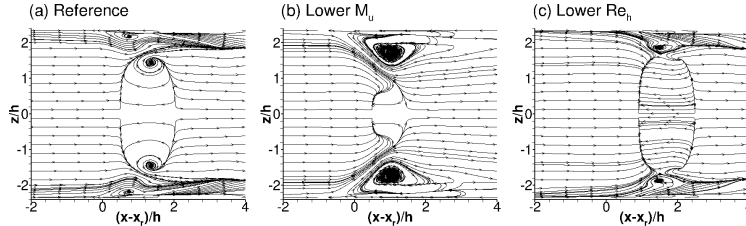


**Fig. 9** Visualisation of the wall shear stress using friction lines just above the wall

Experimental studies of oblique and normal SWBLIs performed by Dupont et al. [19], Doerffer et al. [20], and Bruce et al. [21] report that the extent of the shock-induced separations at the centreline of the duct is strongly affected by the state of the flow at the corners of the duct. In the experiment by Bruce et al. [21] reduction of the corner separation upstream by suction resulted in a separated region at the centreline in a previously attached flow field. The case at lower Mach number  $M_u$  has larger corner separations and smaller separations on the upper and lower walls. The size of the centreline separation is reduced due to the increase of the corner separations which is in agreement with experiments. Both the reference and low  $Re_h$  case feature an oblique initial shock structure. The case at lower  $M_u$  shows an initial shock with a Mach stem. Such shock structure is observed at low levels of confinement and lower pre-shock Mach numbers  $M_r$ . Considering the reference case and the cases at low  $M_u$  and low  $Re_h$  the pressure recovery  $p_0/p_{0,\infty}$  at  $(x - x_r/h)$  (20 non-dimensional streamwise distances after the onset of the interaction) is highest for the case at low  $M_u$  (0.8253). The difference in pressure recovery between the reference and low  $Re_h$  case is  $\Delta p_0/p_{0,\infty} = 0.005206$ . As

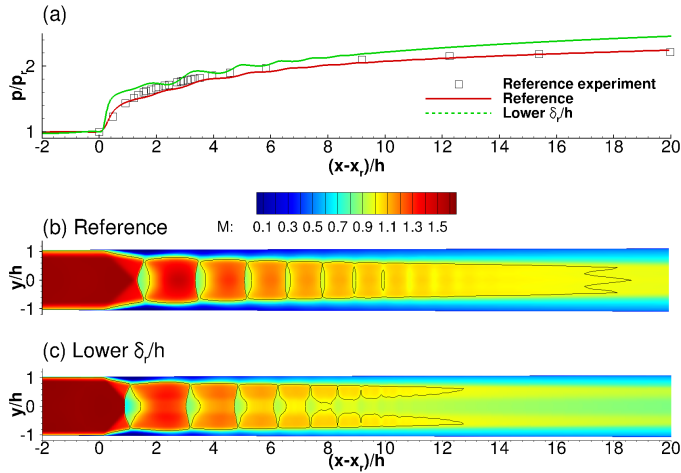


**Fig. 10** Wall pressure (top) and Mach number contours (bottom) for reference and reduced  $\delta_r/h$  cases

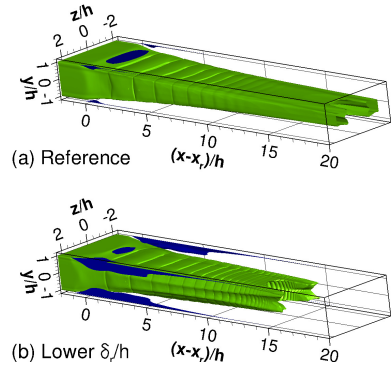


**Fig. 11** Iso-surfaces of  $M = 1.0$  (shaded green) and  $u/V_u = -1 \times 10^{-3}$  (shaded blue) for the reference and reduced  $\delta_r/h$  cases

the outlet pressure is increased by  $\approx 12\%$  for the reference case, the onset of the interaction moves upstream, to  $x_r/h = 15.597767$ . The movement is equivalent to  $\approx 23\%$  of the domain length. Figure 10 shows the wall pressure and Mach number contours for the reference and reduced  $\delta_r/h$  cases. The upstream movement of the shock is accompanied by a reduction of the shock train length and by changes of the initial shock structure. The differences in pre-shock Mach number and confinement between the cases amount to  $\approx 1.3\%$  and  $\approx 36.2\%$ . As the confinement is reduced, the shock train becomes shorter and the spacing between subsequent shocks decreases (Carroll et al. [11]). The case at low  $M_u$  has similar confinement to the case at low  $\delta_r/h \approx 0.19$ .

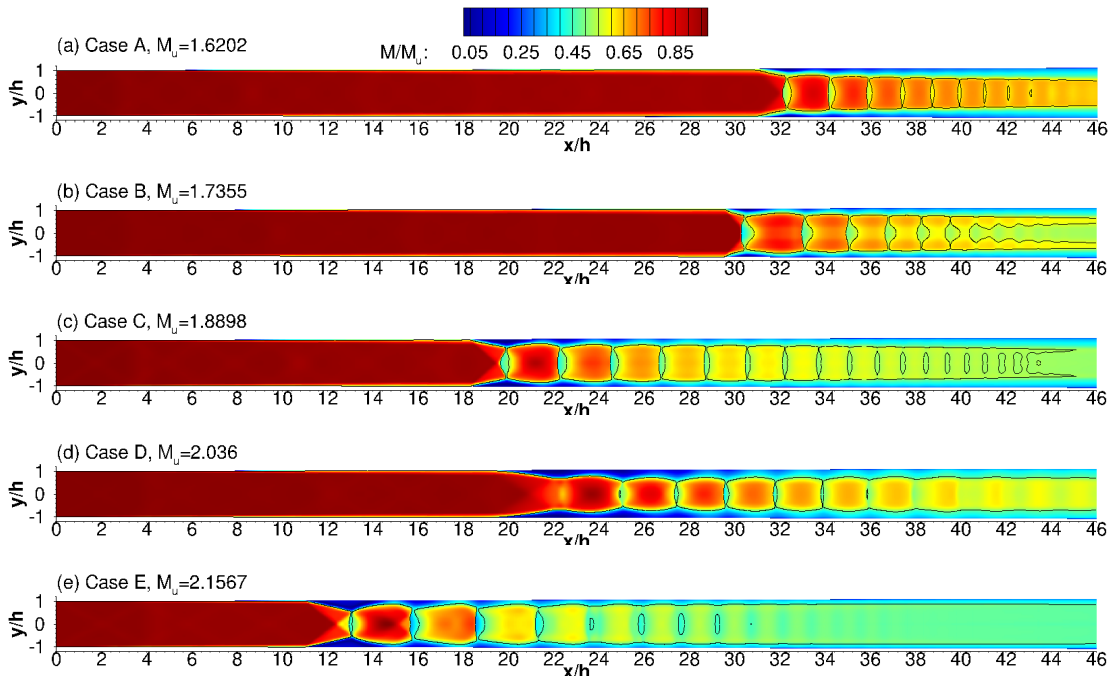


**Fig. 12** Non-dimensional Mach number contours  $M/M_u$  for cases A to E; solid black line represents sonic conditions

The difference in the pre-shock Mach numbers is  $\approx 7\%$ . Nevertheless, both cases feature shorter shock trains with an initial shock that has a Mach stem. The pressure recovery for the  $\delta_r/h$  case is  $p_0/p_{0,\infty} = 0.7834$ , again taken at 20 dimensionless distance units after the start of the interaction. Figure 11 shows the sonic and separation isosurfaces for the reference and low  $\delta_r/h$  cases. For the latter, the corner separations are larger. The size of the corner separation affects the centreline separation and the structure of the initial shock. For cases with larger levels of flow confinement (reference and low  $Re_h$ ), the corner separations are small resulting in a larger separation at the centreline. Both cases show an initial shock without a Mach stem. Figure 12 shows the Mach number contours for the remaining MSWBLI cases - A to E. For the shock train at  $M_u = 1.7355$  (case B) the initial shock features a Mach stem. Absence of a Mach stem is observed for the shock train at  $M_u = 1.6202$  (case A) although the pre-shock Mach number is lower. The difference in the pre-shock Mach number amounts to  $\approx 8\%$ . Comparing the confinement ratios shows that case A has higher confinement ( $\delta_r/h = 0.3606$ ) than case B ( $\delta_r/h = 0.3131$ ). The corner separations for case A are smaller giving rise to a larger centreline separation which affects the initial shock structure. Cases C and E have lower levels of flow confinement than cases A and B. However, the shock train is formed by two crossing oblique shocks followed by a series of normal shocks. According to Matsuo et al. [1] for Mach numbers  $M_u$  greater than 1.8-2.2 oblique shock trains are mostly observed, depending on the state of the boundary layers. The pre-shock Mach number for cases C and E fall within this range. Case C features an initial shock with a bifurcation point very close to the centreline, whereas case E features two crossing oblique shocks terminated by a normal shock. In both cases, the downstream shocks are concave facing upstream. All cases without a distinct bifurcation of the initial shock, i.e. the bifurcation point is closer to the centreline do not have supersonic tongues (reference, low  $Re_h$ , case A, case C, case D). Cases with an initial bifurcated shock where the bifurcation point is below the centerline have supersonic tongues (low  $M_u$ , low  $\delta_r/h$ , case B). The flow near the slip-line emanating from the bifurcation point of the initial shock remains supersonic for longer distances. As these points move closer to the centreline, the core flow after the shock train remains supersonic. Figure 13 shows the relationship between the pressure ratio across the start of the interaction and the outlet  $p/p_r$  and the level of flow confinement  $\delta_r/h$ , the pre-shock Mach number  $M_r$ , and the onset of the interaction  $x_r$ . A linear fit (shown by the solid red lines) is tested here for the variation  $M_r$  and  $\delta_r/h$  with respect to  $p/p_r$ .

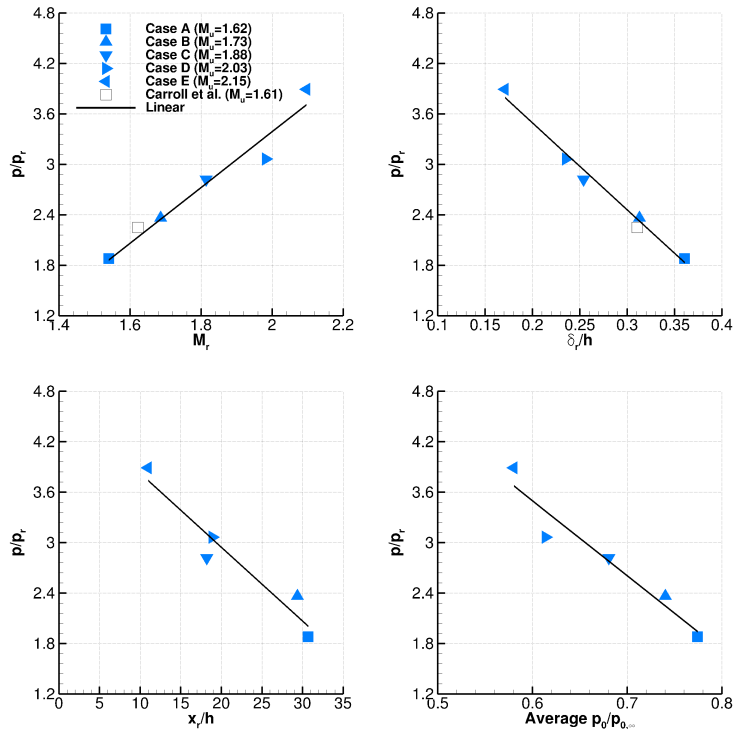


**Fig. 13** Mach number, confinement level, location of the initial pressure rise and average stagnation pressure ratio at the outlet

### 3. Efficiency metrics for MSWBLI

The effect of pseudo-shock length on the total pressure recovery was investigated by Mahoney [22] who showed that maximum total pressure recovery  $p_0/p_{0,\infty}$  is achieved when the throat length equals or is slightly greater than the pseudo-shock length. For maximum total pressure recovery at off-design conditions e.g. increase/decrease of the design Mach number or non-uniform flow due to change in the angle of attack or sideslip, the length of the throat should be sufficient to account for changes in the pseudo-shock length. The efficiency metrics commonly used for intakes are the flow distortion (FD) and the total pressure recovery (TPR). The FD and TPR are given by

$$FD = \frac{p_{0,max} - p_{0,min}}{p_{0,average}}, \quad (2)$$

$$TPR = \frac{p_{0,f}}{p_{0,\infty}}, \quad (3)$$

where  $p_{0,f}$  is the total pressure at the engine face (duct outlet) and  $p_{0,\infty}$  is the total pressure of the free-stream. Table 4 shows the efficiency metrics for all cases. For the reference cases, the efficiency metrics are evaluated at 20 dimensionless distance units after the start of the interaction. The lowest  $M_u$  case has the highest TPR. The TPR for the case at low  $\delta_r/h$  is higher than the reference case although the  $M_u$  is the same. The FD is less for the low  $\delta_r/h$  and low  $M_u$  cases, which feature shorter shock trains with a bifurcated initial shock. This suggests that reducing the confinement ( $\delta_r/h$ ) ahead of the shock train will improve both the TPR and FD metrics. For cases A-E the TPR loss compared to the ideal TPR is  $\approx 11.98\%$  lower, on average. As  $M_u$  is increased the FD also increases. From the above observations, a shock train featuring an initial bifurcated shock is required for low FD and high TPR. This type of shock train is also shorter, which is an advantage since the length of the intake throat section is usually fixed. As outlined previously, for maximum pressure recovery the length of the throat section should be equal or slightly greater than the pseudo-shock length.

**Table 4 Shock train parametric cases**

Case	$TPR_{ideal}$	$TPR$	$FD$
Ref.	0.8599	0.7576	0.6442
Ref. Low $M_u$	0.8989	0.8253	0.5157
Ref. Low $Re_h$	0.8599	0.7628	0.6550
Ref. Low $\delta_r/h$	0.8599	0.7834	0.5732
A	0.8876	0.7741	0.6605
B	0.8408	0.7401	0.6859
C	0.7721	0.6805	0.7452
D	0.7040	0.6138	0.9382
E	0.6480	0.5802	0.7862

## IV. Simulation of shock trains in the context of high-speed intakes

This section will focus on an approximate square intake with a fore-body. Inside the intake, compression is achieved by a series of shocks and its performance is influenced by the free-stream  $M_\infty$ ,  $Re_\infty$  and downstream (engine face) conditions. It is of interest to quantify the pressure recovery, mass flow rate, and flow-distortion for such a complex case.

### A. Fore-body intake geometry

Since the flow is supersonic only a fore-body with intake is considered for simulations. Figure 14 shows the employed geometry of the fore-body with an intake. The fore-body is made up of a tangent ogive of length  $0.3L$  followed by a cylinder of length  $0.7L$ . The internal compression intake features a square profile of  $2h = 2w = 0.05L$  and thickness of  $t = 0.003L$ . The gap between the fore-body and the intake (the diverter) is  $0.1L$ , the intake is oriented at 45 deg to the fore-body symmetry plane and it extends another  $0.2L$  after the fore-body. The employed aspect ratio of one, the 45 deg angle and the placement of the intakes on the windward side contribute to higher pressure recovery as

stated by Goldsmith [23]. The diverter height of  $0.01L$  ( $0.1D$ ), where  $D$  is the fore-body diameter, is sufficient to keep the negative effect of sideslip angle on the pressure recovery and mass flow ratio small (Goldsmith [23]).

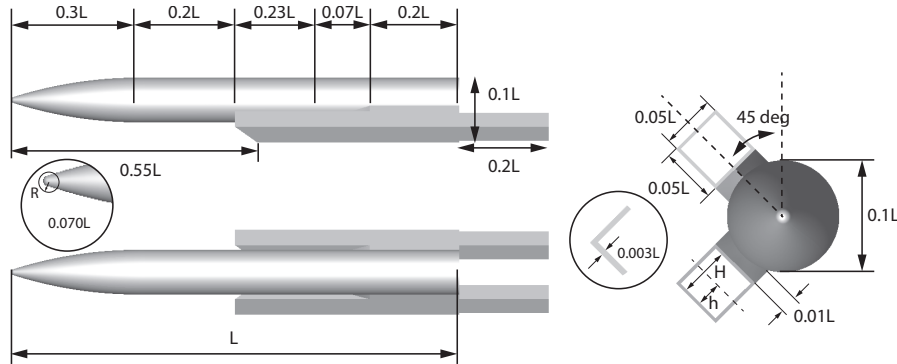


**Fig. 14 Fore-body intake geometry**

The intake and body are not optimised for pressure recovery are used here for demonstrating the potential application of the CFD method to a more complex case.

### B. Numerical setup

The computational domain is non-dimensionalised with the fore-body length  $L$ . For cases at zero roll angle, only half of the domain is considered with symmetry boundary conditions applied at the  $x$ - $z$  plane. Free-stream boundary conditions were applied at the far-field boundaries and extrapolation boundary conditions (except where the flow is subsonic) were applied at the engine face. Both O- and H-topologies were used for the multiblock structured grid. An O-topology was used around the intake and the fore-body and an H-topology was employed inside the intake. Adiabatic wall boundary condition was imposed at the surface of the fore-body intake. Figure 15 shows the computational domain boundaries (left) and the far-field (middle) and nearfield (right) grid topology. Table 5 shows the grid parameters.

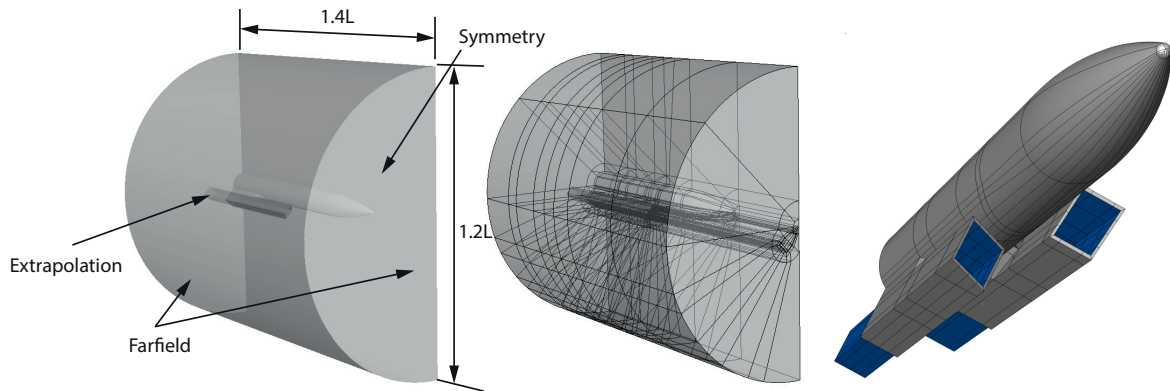


**Fig. 15 Fore-body intake domain boundaries and computational grid topology**

Around the fore-body, the first cell spacing was set to  $1.0 \times 10^{-6}L$  to ensure a non-dimensional distance of  $y^+ \leq 1$ . Considering the results from the MSWBLI validation section, the maximum and minimum  $y$  and  $z$  cell spacings within the intake were set to  $0.001L$  and  $2.5 \times 10^{-7}L$  which when scaled to the intake half-height ( $h = 0.025L$ ) translate to  $0.04h$  and  $1 \times 10^{-5}h$ .

**Table 5 Fore-body intake simulation grids; distances are non-dimensional**

Grid	Fore-body wall distance	Intake wall distance	Points
A	$1.0 \times 10^{-6}$	$2.5 \times 10^{-7}$	$34.17 \times 10^6$

For all simulations, the free-stream Mach number was set to  $M_\infty = 2.0$  to promote the formation of multiple SWBLIs in the intake. At this Mach number, the intake is self-starting as the ratio of the throat area to inlet area is greater than the Kantrowitz limit (0.8220). The Reynolds number based on the length of the fore-body was set to  $Re = 20 \times 10^6$ . This gave a Reynolds number based on the intake half-height of  $Re_h = 5 \times 10^5$  since  $h = 0.022L$ . The turbulence intensity and eddy-viscosity ratio at the far-field were set to  $I_\infty = 0.01$  (1%) and  $\frac{\mu}{\mu_\infty} = 10$ . The outlet pressure was set to 75% of the pressure downstream of a normal shock at a free-stream Mach number of  $M_\infty = 2.0$ . The pressure rise across a normal shock at a pre-shock Mach number of  $M_\infty$  is given by

$$\frac{p}{p_\infty} = 0.75 \frac{(2\gamma M_\infty^2 - (\gamma - 1))}{(\gamma + 1)} \quad (4)$$

where  $\gamma$  is the ratio of specific heats (1.4) and the 0.75 factor gives the 75% rise of pressure. The fully turbulent  $k-\omega$  EARSM turbulence model was used for all cases due to its consistent prediction of the multiple shock wave boundary layer interactions experiments reported in section III. Table 6 shows the parameters for the fore-body intake simulations.

**Table 6 Fore-body intake simulation parameters**

Grid	$I_\infty$ %	$M_\infty$	$\alpha$ deg	$\beta$ deg	Avg. $y^+$	FD	$p/p_\infty$	Turbulence model
A	1.0	2.00	0.0	0.0	0.5005	0.5056	3.3750	$k-\omega$ EARSM

All cases were initialized with free-stream conditions everywhere in the domain apart from the very end of the intake, where conditions after a normal shock at a pre-shock Mach number of  $M_\infty = 2.0$  were specified.

### C. Results and discussion

Figure 16 shows the non-dimensional surface pressure and the  $M = 1$  and  $u/V_\infty = -1 \times 10^{-3}$  iso-surfaces. At the location of the MSWBLI, four corner separations can be observed with no separation at the centreline. Small centreline separation is observed at the location of impingement of the oblique SWBLI created by the lower intake wall. Figure 17 shows wall pressure (a) and Mach number contours (b-c) at the two orthogonal midplanes of the intake. The lower intake wall promotes the formation of an oblique SWBLI. The oblique SWBLI impinges on the boundary layer developing on the top wall. The increase of upper wall pressure at  $(x - x_o)/h \approx 4.1$  indicates the location of impingement of the oblique SWBLI. The subsequent reflections of the oblique SWBLI interact with the MSWBLI formed downstream. The MSWBLI features an initial bifurcated shock wave (identifiable Mach stem), thus it can be classified as a normal MSWBLI.

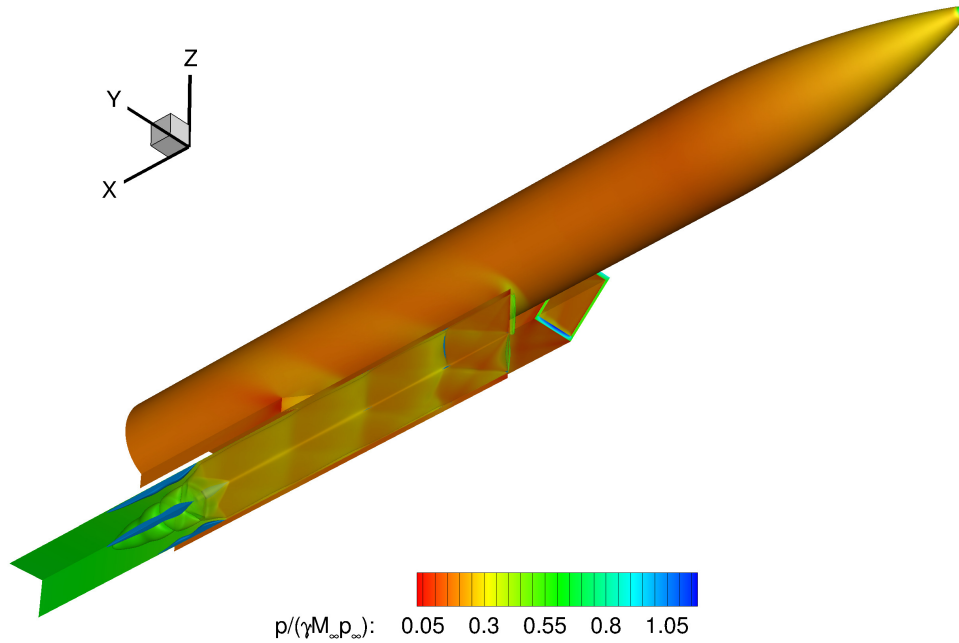
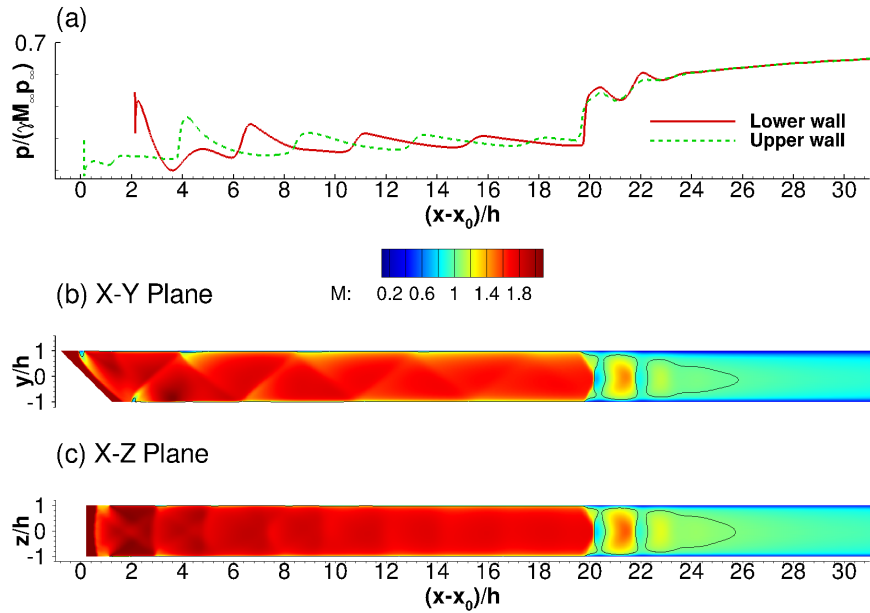


**Fig. 16 Non-dimensional surface pressure and sonic isosurface, along with regions of reversed flow  $u/V_\infty = -1 \times 10^{-3}$  in blue**

The shock train does not exhibit symmetry across the  $x$ - $y$  plane of the intake which is evident by the sonic line (solid black). Additionally from Figure 17 (b) and (c) two shocks can be identified. Supersonic tongues observed previously in the isolated MSWBLI cases are absent. The absence of the tongues can be attributed to the smaller Mach stem of the initial shock (bifurcation point closer to the centreline). At the centreline, the flow is supersonic up to  $(x - x_0)/h \approx 26$ . This is the location where the pseudo shock ends. The total pressure recovery (TPR) and flow distortion (FD) were evaluated at  $(x - x_0)/h = 31$ . The stagnation pressure was averaged (area-weighted) over the cross-section of the intake at this location. The TPR is 0.63856 which is 11.42% lower than the TPR across a normal shock at pre-shock Mach number of  $M = 2$  ( $p/p_\infty = 0.7209$ ). The MIL-E-5008B relations provide a reasonable initial estimate for the inlet TPR (Mattingly et al. [24]). Inlet TPR as a function of the  $M_\infty$  is given by

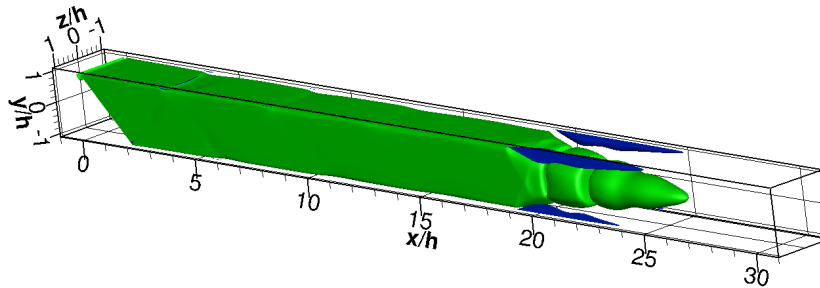
$$\eta_{spec} = 1 - 0.075 (M_\infty - 1)^{1.35}, \quad 1 < M_\infty < 5 \quad (5)$$

which gives 92.5 TPR % at  $M_\infty = 2.0$ . The actual inlet TPR is usually less.



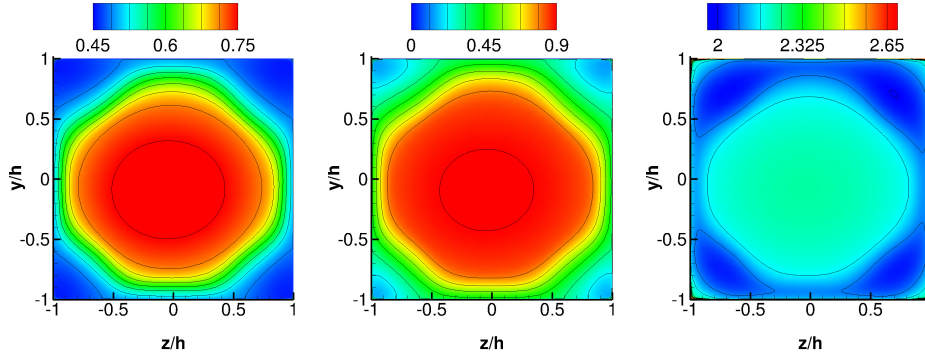
**Fig. 17** Wall pressure and Mach number contours for the fore-body intake

Figure 18 shows the sonic ( $M = 1$ ) and separation ( $u/V_\infty = -1 \times 10^{-3}$ ) iso-surfaces. There are four corner separations within the intake, beginning at  $(x - x_0)/h \approx 19$ . The isolated shock train simulations showed that for larger corner separations there is no separation at the centreline which often leads to an initial shock featuring a Mach stem. Due to the relative size of the corner separation to the intake cross-section, no separation at the centreline is observed. The corner separations at the upper wall are more pronounced than the ones at the lower, leading to a slightly asymmetrical MSWBLI structure. In addition to the four corner separations, small corner separations are observed upstream of the shock train at the locations of the impingement of the SWBLI, created by the lower intake wall.



**Fig. 18** Sonic  $M = 1$  and separation  $u/V_\infty = -1 \times 10^{-3}$  iso-surfaces for the fore-body intake

Figure 19 shows stagnation pressure, Mach number and streamwise velocity contours at the assumed engine face location  $(x - x_0)/h = 31$ . The contours show that there are no large flow asymmetries with respect to  $y/h = z/h = 0$  at this location. The flow distortion (FD) at  $(x - x_0)/h = 31$  is 0.5056. Using the same definition of FD, the distortion in density is 0.3109



**Fig. 19** From left to right stagnation pressure ratio  $p_0/p_{0,\infty}$ , Mach number  $M$ , and density  $\rho/\rho_\infty$  contours at  $(x - x_0)/h = 31$

Although not very efficient in terms of TPR and FD the employed fore-body and intake geometry serves the purpose of coupling an external flow around a fore-body and internal flow with both oblique and multiple SWBLIs. The predicted initial shock in the shock train features a Mach stem (similar to the low  $M_u$  and low  $\delta_r/h$  cases). However, no supersonic tongues are observed. The flow near the centreline downstream of the shock train remains supersonic (similar to the reference and low  $Re_h$  case). The length of the shock train is considerably less than the shock train length in the isolated cases.

## V. Conclusions and future work

The following conclusions have been drawn from this study:

- The most suitable approach for simulating shock trains is to adjust both the Mach number at the inlet of the domain and the pressure at the outlet of the domain to match the Mach number  $M_r$  and confinement  $\delta_r/h$  before the interaction.
- Eddy-viscosity models exhibit overprediction of the corner separations which in turn suppress the centreline separations. This often leads to the supersonic core flow being predicted closer to the wall resulting in pressure oscillations at the wall.
- Due to its capability of resolving the secondary (corner) flows the  $k-\omega$  Explicit Algebraic Reynolds Stress Model (EARSM) predicts smaller corner separation and results in a slight underprediction of the wall pressure with no pressure oscillations.
- For the reference case considered, reduction of confinement results in a shorter shock train and larger corner separations. The larger corner separations lead to a smaller separation at the centreline and an initial shock with a bifurcation point below the centreline. Reduction of the upstream Mach number has a similar effect, with the effect of Mach number on the length of the shock train being more pronounced. An opposite trend is observed for the reference case and the reduced Reynolds number case. For both cases, the confinement is larger with smaller corner flows and larger centreline separation leading to an initial shock with a bifurcation point close to the centreline. The core flow after the shock train, of the cases with no distinct bifurcation point below the centreline, is supersonic. Cases with bifurcation point below the centreline feature supersonic tongues and subsonic core flow.
- Efficiency metrics using stagnation pressure, have been defined. The metrics give the total pressure recovery across the SWBLI and the flow distortion at stations downstream of the SWBLI. The shorter shock trains, featuring an initial bifurcated shock with a bifurcation below the centreline result in higher TPR and lower FD.
- Both the oblique SWBLI and the multiple SWBLI are present inside the intake. The flow being deflected by the lower wall of the intake forms an oblique SWBLI and its reflection from the upper wall interacts with the multiple SWBLI downstream. The predicted pseudo-shock length is smaller compared to the length of isolated pseudo-shocks at a similar Mach number.
- Flow asymmetry in the form of larger corner separations on the upper intake wall is observed. This shows that for the forebody-intake case flow symmetry cannot and should not be expected as in the isolated cases at similar

Mach numbers.

Future work will include a parametric study of the fore-body intake, considering changes in the free-stream parameters and changes in the geometry, including but not limited to variations in the intake aspect ratio, intake length, and diverter height.

## Acknowledgments

The financial support from MBDA UK is gratefully acknowledged.

## References

- [1] Matsuo, K., Y., M., and Kim, H.-D., "Shock train and pseudo-shock phenomena in internal gas flows," *Progress in Aerospace Sciences*, Vol. 35, 1999, pp. 33–100.
- [2] Handa, T., and Masuda, M., "Three-Dimensional Normal Shock-Wave/Boundary-Layer Interaction in a Rectangular Duct," *AIAA Journal*, Vol. 43, No. 10, 2005, pp. 2182–2187.
- [3] Steijl, R., Barakos, G. N., and Badcock, K., "A framework for CFD analysis of helicopter rotors in hover and forward flight," *International Journal for Numerical Methods in Fluids*, Vol. 51, No. 8, 2006, pp. 819–847.
- [4] Steijl, R., and Barakos, G. N., "Sliding mesh algorithm for CFD analysis of helicopter rotor-fuselage aerodynamics," *International Journal for Numerical Methods in Fluids*, Vol. 58, No. 5, 2008, pp. 527–549.
- [5] Osher, S., and Chakravarthy, S., "Upwind schemes and boundary conditions with applications to Euler equations in general geometries," *Journal of Computational Physics*, Vol. 50, No. 3, 1983, pp. 447–481.
- [6] van Leer, B., "Towards the ultimate conservative difference scheme. V. A second-order sequel to Godunov's Method," *Journal of Computational Physics*, Vol. 32, No. 1, 1979, pp. 101–136.
- [7] van Albada, G. D., van Leer, B., and Roberts, W. W., "A Comparative Study of Computational Methods in Cosmic Gas Dynamics," *Astronomy and Astrophysics*, Vol. 108, No. 1, 1982, pp. 76–84.
- [8] Axelsson, O., *Iterative Solution Methods*, 1<sup>st</sup> ed., Cambridge University Press, 1994.
- [9] Wallin, S., and Johansson, A., "An Explicit Algebraic Reynolds Stress Model for Incompressible and Compressible Turbulent Flows," *Journal of Fluid Mechanics*, Vol. 403, 2000, pp. 89–132.
- [10] Hellsten, A., "New Advanced k-omega Turbulence model for High-Lift Aerodynamics," *AIAA Journal*, Vol. 43, No. 9, 2005, pp. 1857–1869.
- [11] Carroll, B., "Numerical and Experimental Investigation of Multiple Shock Wave/Turbulent Boundary Layer Interactions in a Rectangular Duct," Ph.D. thesis, University of Illinois at Urbana-Champaign, Urbana, IL, 1988.
- [12] Carroll, B., and Dutton, J., "An LDV Investigation of a Multiple Normal Shock Wave/Turbulent Boundary Layer Interaction (AIAA-89-0355)," *Proceedings of the 27th Aerospace Sciences Meeting*, Reno, Nevada, 1989.
- [13] Carroll, B., and Dutton, J., "Characteristics of Multiple Shock Wave/Turbulent Boundary-Layer Interactions in Rectangular Ducts," *Journal of Propulsion and Power*, Vol. 8, No. 2, 1992, pp. 441–448.
- [14] Carroll, B., and Dutton, J., "Multiple normal shock wave/turbulent boundary-layer interactions," *Journal of Propulsion and Power*, Vol. 8, No. 2, 1992, pp. 441–448.
- [15] Carroll, B., and Dutton, J., "Multiple normal shock wave/turbulent boundary-layer interactions," *AIAA Journal*, Vol. 30, No. 1, 1992, pp. 43–48.
- [16] Carroll, B., Lopez-Fernandez, P., and Dutton, J., "Computations and Experiments for a Multiple Normal Shock/Boundary-Layer Interaction," *Journal of Propulsion and Power*, Vol. 9, No. 3, 1993, pp. 405–411.
- [17] Sun, L., Sugiyama, H., K., M., Hiroshima, T., and Tojo, A., "Numerical and experimental study of the Mach 2 pseudo-shock wave in a supersonic duct," 2005.

- [18] Fievet, R., Koo, H., and Raman, V., “Numerical Investigation of Shock-Train Response to Inflow Boundary-Layer Variations,” *AIAA Journal*, Vol. 55, No. 9, 2017, pp. 2888–2900.
- [19] Dupont, P., Haddad, C., and Ardissonne, J., J.-P. Debieve, “Space and time organisation of a shock wave/turbulent boundary layer interaction,” *Aerospace Sciences and Technology*, Vol. 9, No. 1, 2005, pp. 561–572.
- [20] Doerffer, P., Hirsch, C., Dussauge, J., Babinsky, H., and Barakos, G., *Unsteady Effects of Shock Wave Induced Separation: 220 (Notes on Numerical Fluid Mechanics and Multidisciplinary Design)*, 1<sup>st</sup> ed., Springer, 2011.
- [21] Bruce, P., H., B., Tartinville, B., and Hirsch, C., “Corner Effect and Asymmetry in Transonic Channel Flows,” *AIAA Journal*, Vol. 49, No. 11, 2011, pp. 2382–2392.
- [22] Mahoney, J., *Inlets for supersonic missiles (AIAA Education Series)*, 1<sup>st</sup> ed., American Institute of Aeronautics and Astronautics, 1990.
- [23] Goldsmith, E., and Seddon, J., *Practical Intake Aerodynamic Design (AIAA Education Series)*, 1<sup>st</sup> ed., American Institution of Aeronautics and Astronautics, 1993.
- [24] Mattingly, J., Heiser, W., and Daley, D., *Aircraft Engine Design (AIAA Education Series)*, 2<sup>nd</sup> ed., American Institute of Aeronautics and Astronautics, 2002.